Configuration design and experimental verification of a variable constant-force compliant mechanism

Bingxiao Ding[1], Xuan Li[2] and Yangmin Li[1,*]

[1]Department of Industrial and Systems Engineering, The Hong Kong Polytechnic University, Hong Kong, 999077, China and
[2]College of Physics and Electromechanical Engineering, Jishou University, Jishou, 416000, China
*Corresponding author. E-mail: yangmin.li@polyu.edu.hk

Abstract

The realizing of variable output constant force has received wide attention. To achieve a force regulation in an economic way, a configuration of the constant force mechanism (CFM) referring to positive and negative stiffness combination method is proposed in this paper. By adjusting preloading displacement applied on positive-stiffness structure of the CFM, the variable constant force output can be realized. The force–displacement expression of the CFM in the non-preloaded condition is deduced by the established analytical models. Furthermore, parametric sensitivity analysis with several architectural parameters are conducted for optimizing physical structures. Finally, the correctness of the proposed principle is verified by experimental studies. The observed experimental results show that the CFM under different preloading displacements can provide required output constant force, which is consistent with proposed hypothesis.

1. Introduction

Constant force mechanism (CFM) also known as quasi-zero stiffness mechanism, which can perform output a constant force in a certain range of input displacement [1–3]. The CFM that can maintain the output force in a specific value has been widely adopted in application of ultraprecision polishing, micro-manipulation, and vibration isolation [4–6]. Generally speaking, the constant force can be realized by a closed-loop control method with force sensors and advanced algorithms. For instance, Choi et al. adopted a robust force tracking control to improve the performance of SMA-based flexible gripper [7]. Huang et al. reported an automatic cell injection system based on force sensing and controlling method [8]. Zhang et al. developed an automated robotic micromanipulation system with MEMS force sensor for studying the Drosophila larvae [9]. However, the aforementioned method required expensive sensors and complex algorithms which increases the cost of realizing constant force. To reduce the dependency on complicated control algorithms, CFMs consisting with passive elastic structure were presented from the perspective of mechanism design [10, 11].

During the literature review, CFM can be realized by designing a specific curved-beam, shape optimization and stiffness combination methods. For curved-beam-based CFM, the constant force is generated by designing a special shape beam. Wang et al. developed a constant force bistable micro-mechanism with force regulation and overload protection functions [12]. Pedersen et al. designed a compliant mechanism that can deliver a constant output force to modify characteristics of the actuator by topology and size optimization methods [13]. Similar to the curved-beam CFM, the shape optimization CFM generates a constant force output based on meticulously process. For example, Chen et al. presented a constant force clip to overcome snap-fit mating uncertainty relying on shape optimization of a cantilever-like structure [14]. Liu et al designed a compliant constant-force mechanism by topology and geometry optimization methods, which can generate a nearly constant output force over a range
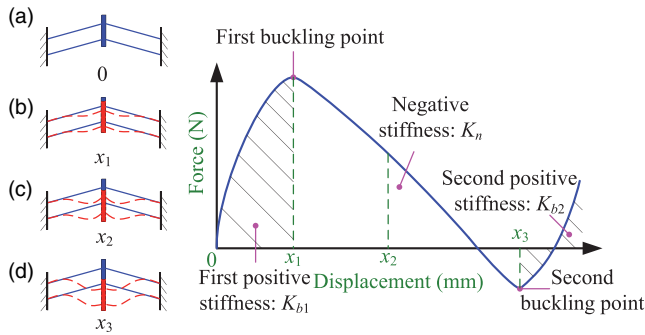
Figure 1. *Force–displacement curve of BSB.*

of input displacements [15]. The difference between the curved beam and shape optimization CFM is that the former referring to fixed-guided beam and the latter based on fixed-free cantilever beam [16]. However, both of curved beam and shape optimization CFM are required to obtain the specific shape by analytical modeling which is a time-consuming process. Different with aforementioned two methods, stiffness-combination CFM obtains constant force by combination of PSS and negative-stiffness structure (NSS) [17]. Ye et al. proposed a type of multistage CFM based on the parallel connection of negative and positive stiffness modules [18]. Liu et al. designed a compliant constant force gripper by using the combination of positive stiffness and negative stiffness mechanism [19]. Compared with curved beam and shape optimization CFMs, the stiffness combination CFM attracted wide attention for the advantages of simple structure, accurate output, and low requirement on materials.

However, in some applications, the changing of constant output force magnitude is desirable. For example, in applications that the initial desired force is unknown and in applications where a system calls for gradual change in output force over a range of motion [20]. Hence, to further expand the application of CFM, the design of variable constant force mechanism (VCFM) could be highly beneficial for these applications. Generally speaking, the variable constant force output can be realized by conventional rigid link mechanism and compliant mechanism. Due to the advantages of frictionless, no backlash, vacuum compatibility and compactness, a compliant VCFM is proposed in this study [21].

The main contribution of this paper is to propose a compliant VCFM with experimental verification. The remainder of this is organised as follows. Section 2 introduces the principle of VCFM realization based on the stiffness combination method. Section 3 presents the comparison of typical PSSs and NSSs, including the design of VCFM. Analytical modeling of positive and negative stiffness structure is established in Section 4. In addition, the sensitivity of structural parameters to constant force property is conducted in Section 5. Furthermore, experimental validation is presented in Section 6. Finally, conclusions are drawn in Section 7.

2. Principle of realization VCFM

To get a variable constant force, the output constant force should be obtained initially. In this paper, the constant force is obtained by combination of a PSS and NSS in parallel. The negative stiffness is generated by BSB with its buckling property, as shown in Fig. 1. Referring to this figure, as increasing the input displacement, the BSB will appear in two stable buckling positions, which correspond to Fig. 1(b) and (d), respectively. The first positive stiffness occurs at the interval $(0, x_1)$; the negative stiffness region locates in the interval (x_1, x_3). When the displacement exceed x_3, it begins to show the second positive stiffness characteristic, where x_2 denotes a random point in the negative-stiffness interval (x_1, x_3). To obtain a zero-stiffness characteristic, the magnitude of positive stiffness K_p and negative stiffness K_n must be equal.
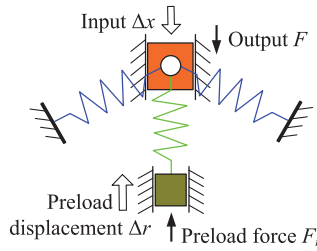
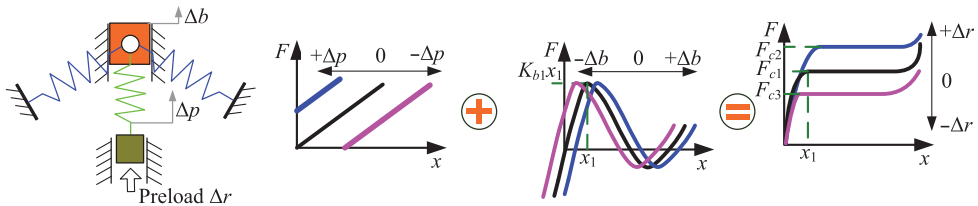**Figure 2.** *The realization principle of VCFM.*

Figure 3. *Force–displacement curves of the VCFM in the different preloading conditions.*

In the interval of (x_1, x_3), the output constant force F_{c1} can be derived referring to stiffness combination method:

$$F_{c1} = (K_p + K_{b1})x_1 \tag{1}$$

where K_{b1} denotes the value of first positive stiffness.

To realize variable constant output force, it means to regulate the magnitude of F_{c1} with ΔF_c, namely $F_{c1} \pm \Delta F_c$. Referring to the Eq. (1), the force adjusting can be realized by two methods. One is to adjust the value of $K_p + K_{b1}$. However, the changing in stiffness involves massive workload and the difficulty to realize. The other method is to adjust the value of x_1 to the mechanism that is adopted in this paper.

The principle of applying a preloading displacement to realize variable constant force output is depicted in Fig. 2, where the symmetric BSBs and a linear spring are connected in parallel [22]. The end of the linear spring is connected to the preloading device to provide a preload force F_r (or preload displacement Δr) enabling the linear spring in pretightened condition. Simultaneously, the BSB will move upward when subjected to the preload force, but its deformation displacement is relatively small compared to the linear spring. Through applying prior preloading force, the output constant force can be regulated accordingly. In order to give a further explanation of this principle, force–displacement curve of the CFM in the different preloading conditions is shown in Fig. 3.

Referring to this figure, when a preload displacement $\pm\Delta r$ is applied, the positive-stiffness curve moves along x-axis in negative or positive direction with Δp, and a reaction force $K_p\Delta p$ generates accordingly. The force–displacement curve of the BSB moves along x-axis in positive or negative direction with Δb, and a reaction force $\mp K_{b1}\Delta b$ generates in the initial state. In accordance with $\Delta r = \Delta p + \Delta b$, the following equations can be obtained:

$$K_p\Delta p = K_{b1}\Delta b \tag{2}$$

$$F_{c2} = K_p(x_1 + \Delta r) + K_{b1}x_1 \tag{3}$$

$$F_{c3} = K_p(x_1 - \Delta r) + K_{b1}x_1 \tag{4}$$

where F_{c2} and F_{c3} are the output constant force of the VCFM in $\pm\Delta r$ preloading displacement. Particularly, the changing of constant force magnitude ΔF_c is merely dependent on the applied preloading displacement on the linear spring. The actual numerical value of the changed constant force is the product of the positive stiffness and the preload displacement, namely $K_p\Delta r$. Meanwhile, the starting
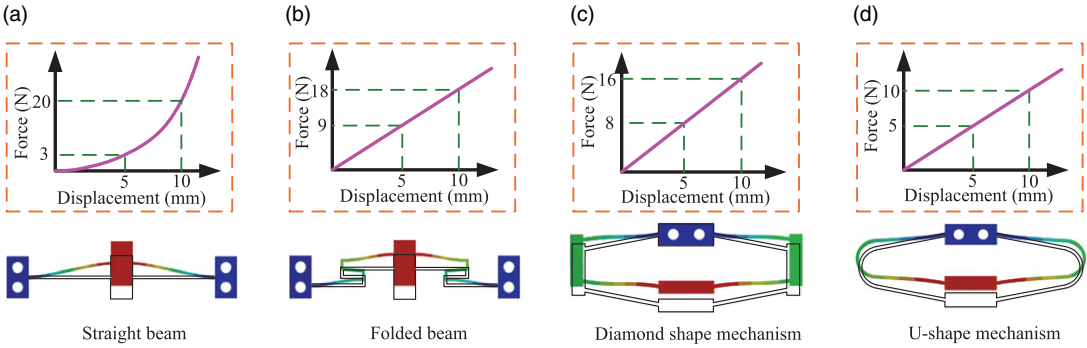
Figure 4. *Comparison of typical PSSs.*

position of the constant force is directly related to the predeformation Δb of the BSB. According to Eq. (3), the following equations can be derived as

$$\Delta r = \frac{F_{c2} - (K_p + K_{b1})x_1}{K_p} \tag{5}$$

$$\Delta b = \frac{K_p \Delta r}{K_p + K_{b1}} \tag{6}$$

Therefore, for a specific constant force, the required preload displacement can be derived by Eq. (5). Furthermore, through the given preloading displacement $+\Delta r$, the magnitude and the starting position of constant force can be deduced by Eqs. (3) and (6), respectively.

3. Design of VCFM

In this section, the designed VCFM is introduced including the comparison of some typical PSSs and BSBs.

3.1. Comparison of PSSs

As introduced in Section 2, the output force regulation can be realized by adjusting the preload displacement applied on the linear spring. For a specific CFM, the PSS denotes linear spring. Hence, choosing a suitable PSS is important for the realization of VCFM. Figure 4 presents the comparison of force–displacement curves of four typical PSSs via Workbench software. The straight beam exhibits highly nonlinear characteristics due to the stress stiffening. It is not suitable to act as a PSS because it cannot ideally neutralize the negative stiffness region of the bistable mechanism [23]. The folded beam exhibits good linear characteristics, but it is not suitable to apply preloading displacement in the input-displacement direction. The diamond-shape mechanism is similar to the U-shape mechanism in geometry shape. The difference is that the U-shape mechanism uses a flexible arc to connect flexible rods, and the diamond-shape mechanism uses a rigid rod. Considering the deformation of the flexible arc, the U-shape mechanism is more prone to fatigue failure [24]. In addition, the analytical model for the U-shape is much complex than the diamond-shape mechanism. Therefore, the diamond-shape mechanism is chosen as a PSS for the designed VCFM.

3.2. Comparison of BSBs

Generally speaking, the typical structural types of BSBs are V-shaped beam, cosine beam, and rigid-flexible hybrid beam, as shown in Fig. 5. The cosine beam exhibits better linearity in the negative stiffness
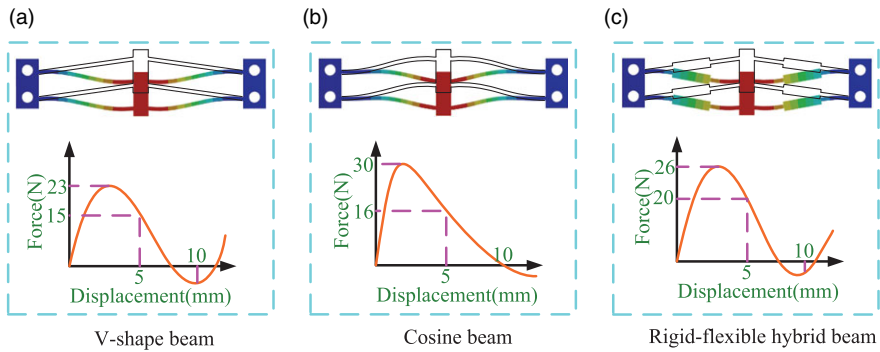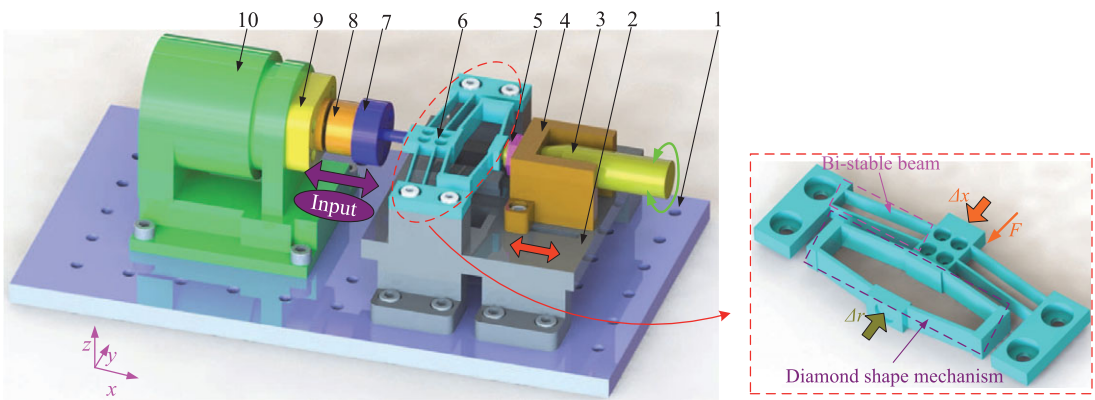
Figure 5. *Comparison of typical BSBs.*

Figure 6. *3D model of the VCFM. 1-antivibration stage, 2-working stage, 3-micrometer head, 4-base, 5-tightening nut, 6-VCFM, 7-connector 1, 8-force sensor, 9-connector 2, 10-voice coil motor.*

stroke than other kind bistable beams. However, the complicated cosine shape beam requires exact pre-stressing that results it difficult to meet different work conditions [25, 26]. V-shaped beam exhibits similar negative-stiffness characteristics to rigid-flexible hybrid beam [27]. Owing to its advantages of simple structure and easy modeling, V-shaped beam is chosen as the NSS to utilize in the CFM design.

3.3. Mechanical design

The 3D model of the designed VCFM is depicted in Fig. 6. The voice coil motor is utilized to provide driven force, and a force sensor is adopted to measure the reaction force. To adjust the preloading displacement directly and easily, the micrometer head is used as a preloaded device which is fixed on the base by a tightening nut. In addition, the base is mounted on the working stage through sliding grooves. Therefore, the assembly errors can be compensated by driving the micrometer head to move along x direction linearity. The preloading displacement Δr applied on the diamond- shape mechanism is realized by adjusting the micrometer head. The displacement Δx at the end of the connector is generated by driven force F.
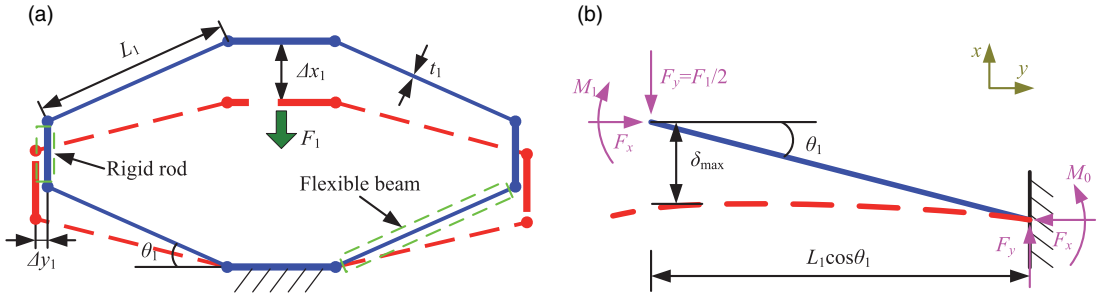
Figure 7. *Modeling of diamond-shaped mechanism: (a) schematic diagram of mechanism deformation, (b) modeling of inclined cantilever beam.*

4. Analytical modeling

To obtain the force–displacement relationship of the designed VCFM, analytical model of the positive and negative stiffness structure is established in this section.

4.1. Modeling of PSS

As shown in Fig. 7(a), the diamond-shaped mechanism consists of four uniformed flexible beams and rigid rods. In this figure, where L_1 denotes length of the flexible beam, t_1 represents width of the flexible beam, θ_1 is angle between the flexible beam and the horizontal plane, Δy_1 is the output displacement, and F_1 is the output force. The deformation of the diamond-shape mechanism can be calculated by superimposing the deformation of each section of the inclined flexible beam. When the deformation of one beam is studied, the other beams can be regarded as ideal rigid bodies. Considering the symmetric characteristic of the structure, the modeling of quarter diamond-shape mechanism is shown in Fig. 7(b).

Referring to Fig. 7(b), the following equation can be deduced as

$$2(M_0 - M_1) = F_x L_1 sin\theta_1 - F_y L_1 cos\theta_1 \tag{7}$$

Furthermore, the following relationship can be obtained:

$$\frac{F_x(L_1 cos\theta_1)^2}{2EI} - \frac{M_1 L_1 cos\theta_1}{EI} = 0 \tag{8}$$

$$\frac{F_x(L_1 cos\theta_1)^3}{3EI} - \frac{M_1(L_1 cos\theta_1)^2}{2EI} = \delta_{max} \tag{9}$$

where δ_{max} is the maximum deformation of the beam, E is the Young's modulus, $I = b_1 t_1^3/12$ is the inertia moment, and b_1 is the out-plane width of the mechanism. δ_{max} is composed of the deformation δ_{bm} caused by the bending moment and the deformation δ_s caused by the shear, namely:

$$\delta_{max} = \delta_{bm} + \delta_s \tag{10}$$

According to Hook's law $F = k\delta$, the following equation can be derived:

$$\frac{1}{k_{max}} = \frac{1}{k_{bm}} + \frac{1}{k_s} \tag{11}$$

The maximum deflection due to bending moment can be expressed as

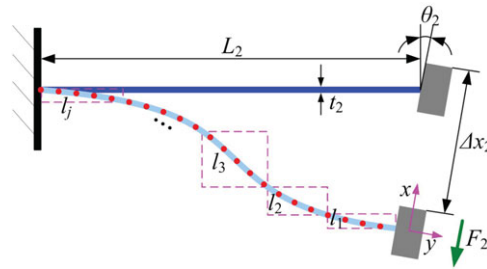$$\delta_{bm} = \frac{F_1(L_1 cos\theta_1)^3}{12EI} \tag{12}$$
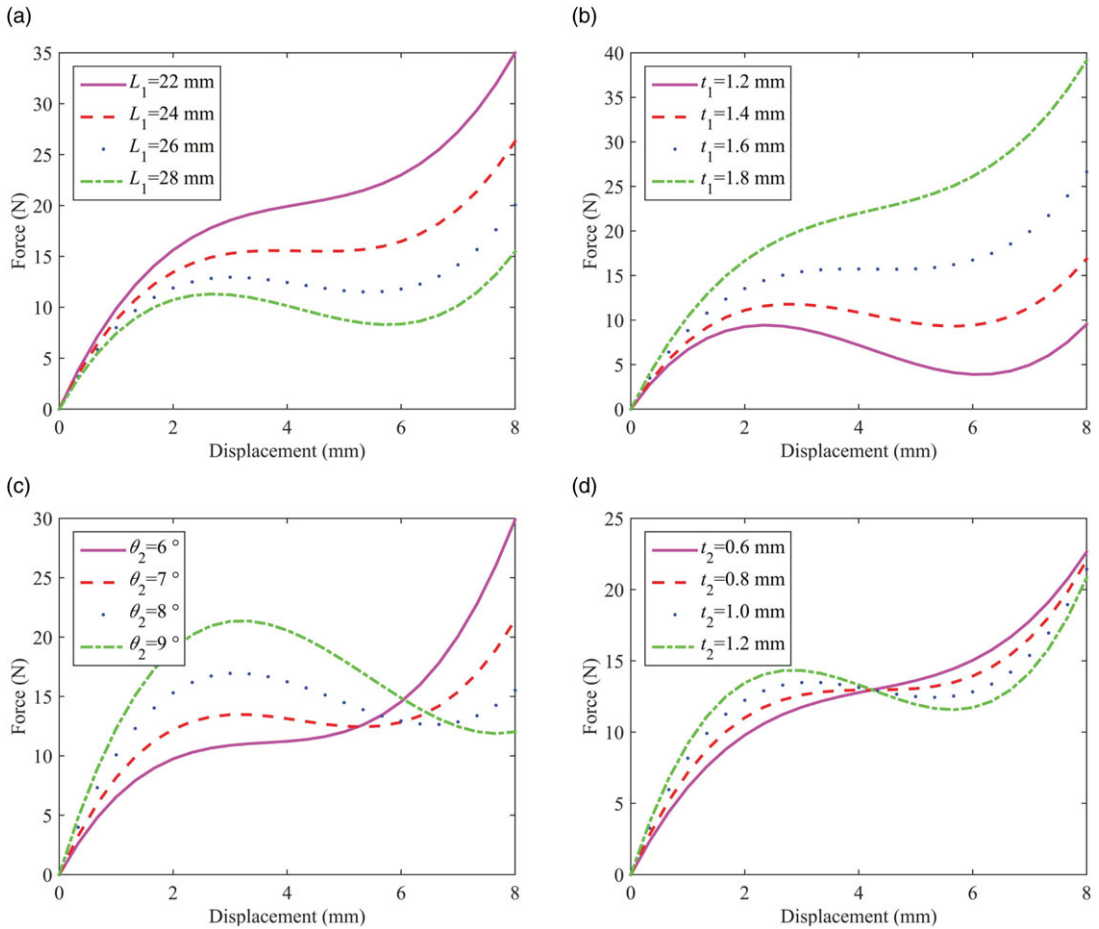
Figure 8. *Modeling of BSB.*

Figure 9. *Parametric sensitivity analysis of the CFM: (a) L_1, (b) t_1, (c) θ_2, (d) t_2.*

The deformation caused by the shear force can be written as

$$\delta_s = \frac{6(1+\mu)F_1 L_1 cos\theta_1}{5EA} \tag{13}$$

where $A = b_1 t_1$ is the cross-sectional area of the beam. According to Eq. (10), the maximum deformation can be derived as

$$\delta_{max} = \frac{F_1(L_1 cos\theta_1)^3}{12EI} + \frac{6(1+\mu)F_1 L_1 cos\theta_1}{5EA} \tag{14}$$

Table I. *Architectural parameters of the VCFM.*

Parameter	Value	Unit
L_1	25.0	mm
θ_1	7	deg
t_1	1.5	mm
b_1	10	mm
L_2	35.0	mm
θ_2	7	deg
t_2	1	mm
b_2	6	mm

Therefore, the force–displacement expression of the diamond-shaped mechanism is

$$F_1 = \left(\frac{2(L_1 cos\theta_1)^3}{Eb_1 t_1^3} + \frac{12(1+\mu)F_1 L_1 cos\theta_1}{5Eb_1 t_1} \right)^{-1} \Delta x_1 \tag{15}$$

4.2. Modeling of BSB

As shown in Fig. 8, when applied an input displacement Δx_2, the corresponding output force F_2 is generated. L_2 and t_2 are the length and width of the BSB, respectively, and θ_2 represents the inclination angle between the horizontal plane and the beam.

Referring to ref. [28], the j_{th} buckling force can be expressed as

$$F_j = \frac{4EI_d \lambda_j^2}{l_j^2} \tag{16}$$

where $I_d = b_2 t_2^3 / 12$ is the inertia moment, and l_j is the length at the j_{th} critical segment, $\lambda_j = \pi, 4.493, 2\pi..., j = 1, 2, 3....$. The negative-stiffness expression of the BSB can be deduced as

$$k_n \approx \frac{33EI_d}{L_2^3} \tag{17}$$

In accordance with Eqs. (11) and (12), the following equation can be deduced by

$$F_2 = ES\frac{\Delta x_2}{L_2} \left(\frac{\Delta x_2}{L_2} - sin\theta_2 \right) \left(\frac{\Delta x_2}{L_2} - 2sin\theta_2 \right) \tag{18}$$

where $S = b_2 t_2$ is the cross-sectional area of the beam. From Eqs. (10) and (13), the fundamental force–displacement formula of the CFM in the nonpreloaded condition can be obtained:

$$F = \frac{Eb_1 t_1^3 \Delta x}{2(L_1 cos\theta_1)^3} + ES\frac{\Delta x_2}{L_2} \left(\frac{\Delta x_2}{L_2} - sin\theta_2 \right) \left(\frac{\Delta x_2}{L_2} - 2sin\theta_2 \right) \tag{19}$$

5. Sensitivity analysis

In general, the more flatness and larger stroke of constant-force output, the better the performance of CFM. To find an optimal solution of parameters, the analysis of structural parametric sensitivity of CFM is conducted.

To analyze the parametric sensitivity of constant-force performance, a series of force displacement curves, related to L_1, t_1, θ_2, and t_2, are depicted in Fig. 9. Referring to this figure, some conclusions can be summarized as follows: Firstly, the length of L_1 varies gradually from 22 to 28 mm with a 2 mm interval. The variation tendency of L_1 is positively correlated to the travel range of the constant force, meaning that the larger the L_1 becomes, the longer the constant-force travel range. However, the amplitude of force is inversely proportional to L_1. In addition, the smaller the L_1, the greater the influence of L_1 exists on the force. Secondly, t_1 of the diamond-shaped mechanism increases from 1.2 to 1.8 mm with an interval
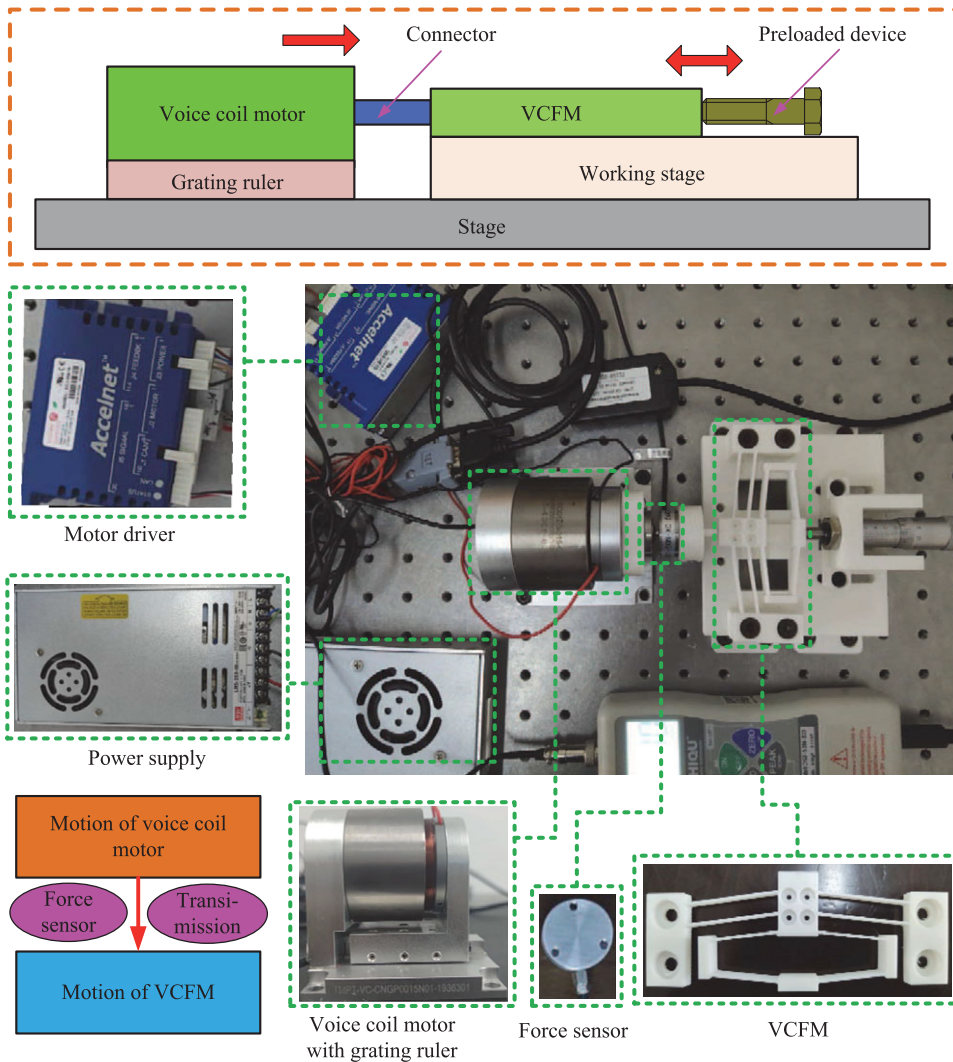
Figure 10. *Experimental setup.*

of 0.2 mm. It is seen that the force increases as t_1 increases. The relationship between the force and t_1 is approximately direct proportional. Thirdly, θ_2 of the bi-stable beam varies gradually from 6° to 9° with an interval of 1°. It should be pointed that the constant-force travel range becomes larger and larger as θ_2 is increasing. An increase of 1° for θ leads to a force increase of approximately 2 N. Nonetheless, the relationship between the force and θ is not directly proportional. Finally, t_2 of the bistable beam changes gradually from 0.6 to 1.2 mm with a 0.2 mm interval. These observations imply that t_2 has no apparently significant connection with critical buckling positions and ranges, merely making a difference to values of stiffness. The most interesting phenomenon is that multiple force–displacement curves can always intersect at one point. As discussed previously, it can be concluded that θ_2 of the bistable beam has the greatest influence on the constant-force performance.

6. Experimental verification

In this section, experimental setup is established to verify the reliability of designed physical configuration and the correctness of analytical analysis. The VCFM prototype is fabricated with high flexibility
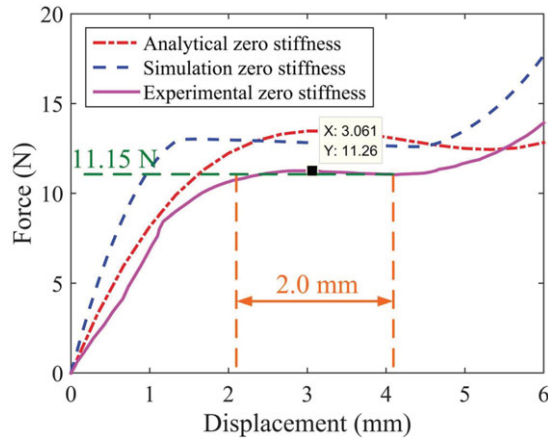
Figure 11. *Comparison of force–displacement curves in non-preload condition.*

material PLA-ST, with its density $\rho = 1250\,\text{kg/m}^3$, Young's modulus $E = 1.477\,\text{GPa}$, and Poisson's ratio $\mu = 0.3$. Referring to the FEA-based optimization method [29], the obtained optimal architectural parameters are shown in Table I.

6.1. Experimental setup

As shown in Fig. 10, a VCFM prototype is fabricated with a 3D printer (model: 3DP-25-4F) to verify the designed concept. The voice coil motor (model: TMEC100-015-000) is driven by a commercial linear servo amplifier (model: ACJ-055-18) to deliver a nominal travel stroke of 10 mm. To measure the reaction force of the mechanism, a force sensor (model: DS2-XD) is mounted at the end of input. A grating ruler (model: LaRW1-3D, Fagor Automation) is integrated to measure the input displacement of voice coil motor. The preload displacement is adjusted by the micrometer head for exhibiting different force–displacement characteristics.

6.2. Experimental results

The comparison of force–displacement curves of obtained experimental data, theoretical and simulation results in non-preloading conditions are depicted in Fig. 11. Referring to this figure, all these curves are exhibiting constant-force property in some degree. The differs of obtained three curves can be explained by following three reasons. First, the size of the finite element meshing process is relatively rough due to the computer performance. Second, the material properties of final printed prototype may be different from the given theoretical values partially because of the printing method and the filling density. Finally, the variation of pretightening force on bolts for fastening VCFM could also lead to the deviation of constant force during the experimental process.

Referring to the experimental data, the output force is ranging from 10.75 to 11.26 N in the interval of [2, 4] mm with an approximate 11.15 N output constant force. The fluctuation value of constant force is 4.5% of the maximum value. Meanwhile, the fluctuation of the force is $+0.11$ and -0.4 N, which is $+0.9\%$ and -3.5% to the average constant force value 11.15 N. Therefore, it meets constant-force definition proposed in the literatures [30]. Furthermore, according to Table II, Eqs. (10) and (13), the positive-stiffness amplitude of the diamond-shaped mechanism K_p is 1.4 N/mm, and the first positive-stiffness amplitude of the BSB K_{b1} is about 5.9 N/mm.

The process to validate the proposed concept is equivalent to verify the correctness of Eqs. (3) and (6). Considering the prototype dimensional size, stretchability, and the rebound limit of the material, the applied preload displacements are 0, 2.5, 5, and 7.5 mm, respectively, as shown in Fig. 12.

Table II. *Comparison of analytical and experimental data.*

Δr	$E\text{-}\Delta F_c$	$A\text{-}\Delta F_c$	Error	$E\text{-}\Delta b$	$A\text{-}\Delta b$	Error
0	0	0	0	0	0	0
2.5	3.79	3.5	7.6%	0.52	0.47	9.6%
5	7.14	7.0	1.9%	1.0	0.95	5%
7.5	10.02	10.5	4.5%	1.45	1.43	1.3%
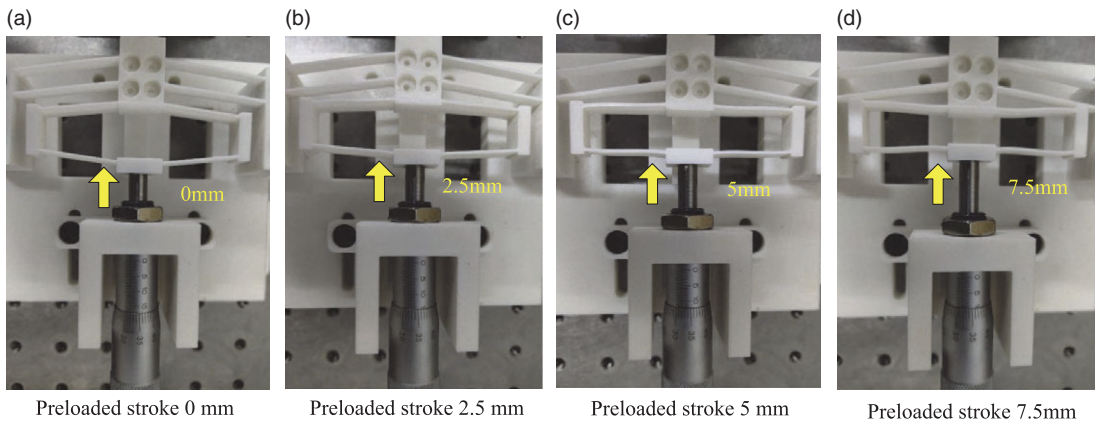
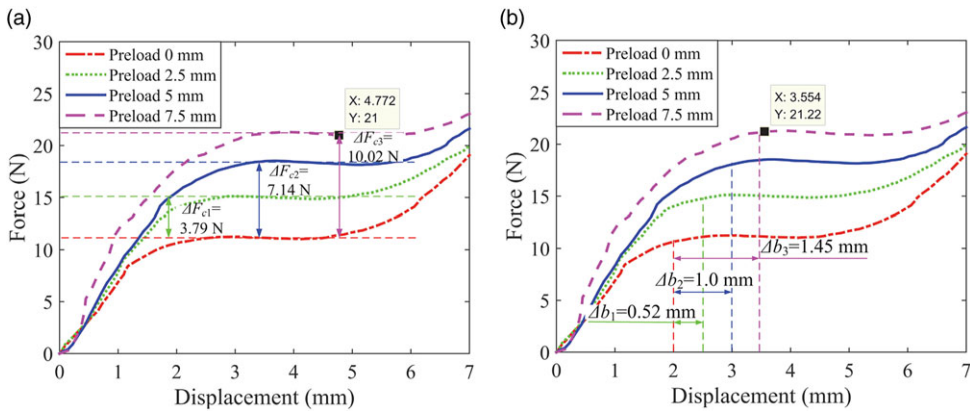***Figure 12.*** *Pictures of different preloaded states.*

Figure 13. *Experimental force–displacement curves in different preload displacements: (a) changing of constant-force; (b) changing of constant-force starting point.*

The force–displacement data responsible for the proposed VCFM are collected in different preloading conditions. The changing of constant force and starting position is shown in Fig. 13 (a) and (b), respectively. When preloading displacement of 0, 2.5, 5, and 7.5 mm are applied, the corresponding constant force is 11.15, 14.94, 18.29, and 21.17 N. The constant force strokes are all close to 2 mm in different preloading conditions. Referring to Eqs. (3) and (6), ΔF_c and Δb can be deduced as illustrated in Table II. The explanation for the error of experimental data ΔF_c and analytical data Δ_b is listed as follows. With the increasing of preloading displacement, the capability of elastic recovery of the mechanism is significantly reduced. In addition, the positive stiffness has changed after several times loading, while the theoretical analysis still believes that the positive stiffness remains constant. Moreover, the first

positive stiffness of the BSB presents noninearity characteristic, whereas theoretical analysis regarded it as a constant value.

7. Conclusions

This paper proposed a configuration type of VCFM referring to the stiffness combination principle. By adjusting the preload displacements on designed diamond-shaped compliant mechanism, the magnitude of output constant force can be easily changed. The mathematical model of PSS and NSS is established according to Hooke's law. The analytical results indicated that the changing of constant force is only related to applied displacement on PSS, and the starting position of constant travel is associated with the predeformation of the BSB. Experimental studies are conducted on the prototype to further validate the correctness of the theoretical analysis. By comparing the experimental and analytical results of ΔF_c and Δb in different preloading conditions, the errors are reasonable and acceptable which are all within 9.6%. The designed VCFM have a potential application in the field that requires force regulation to meet different working environments.

References

[1] V. Parlaktas, "Spatial compliant constant-force mechanism," *Mech. Mach. Theory* **67**(1), 152–165 (2013).
[2] H. X. Wang, J. Zhao, R. J. Gao and Y. T. Yang, "A novel constant-force scanning probe incorporating mechanical-magnetic coupled structures," *Rev. Sci. Instrum.* **82**, 075101 (2011).
[3] L. M. Javier, G. V. Daniel, M. A. C. Francisco and M. G. M. Jose, "Design of three new cam-based constant-force mechanisms," *J. Mech. Design* **140**, 082302 (2018).
[4] T. Zhang, M. Xiao, Y. B. Zou and J. D. Xiao, "Robotic constant-force grinding control with a press-and-release model and model-based reinforcement learning," *Int. J. Adv. Manuf. Technol* **106**(1), 589–602 (2020).
[5] Y. L. Liu and Q. S.Xu, "Design of a Compliant Constant Force Gripper Mechanism based on Buckled Fixed-Guided Beam," **In:** *2016 International Conference on Manipulation, Automation and Robotics at Small Scales (MARSS)* (2016) pp. 1–6. doi: 10.1109/MARSS.2016.7561731.
[6] G. S. Mammano and E. Dragoni, "Mechanical design of buckled beams for low-stiffness elastic suspensions: Theory and application," *Proc. Inst. Mech. Eng. L: J. Mater.: Des. Appl.* **231**(1–2), 140–150 (2017).
[7] S. B. Choi, Y. M. Hua, J. H. Kim and C. C. Cheong, "Force tracking control of flexible gripper featuring shape memory alloy actuators," *Mechatronics* **11**(6), 677–690 (2001).
[8] H. B. Huang, D. Sun, H. Su and J. K. Mills, "Force sensing and control in robot-assisted suspended cell injection system," *Adv. Robot. Virtual Reality* **26**, 61–88 (2012).
[9] W. Zhang, A. Sobolevskl, B. Li, Y. Rao and X. Y. Liu, "An automated force-controlled robotic micromanipulation system for mechanotransduction studies of drosophila larvae," *IEEE Trans. Autom. Sci. Eng.* **13**(2), 789–797 (2016).
[10] M. Li, W. Cheng and R. L. Xie, "Design and experimental validation of a cam-based constant-force compression mechanism with friction considered," *J. Mech. Eng. Sci.* **233**(11), 3873–3887 (2019).
[11] B. Todd, B. D. Jensen, S. M. Schultz and A. R. Hawkins, "Design and testing of a thin-flexure bistable mechanism suitable for stamping from metal sheets," *J. Mech. Design* **132**, 071011 (2010).
[12] D. A. Wang, J. H. Chen and H. T. Pham, "A constant-force bistable micromechanism," *Sens. Actuator A Phys.* **189**, 481–487 (2013).
[13] C. B. W. Pedsresn, N. A. Fleck and G. K. Ananthasuresh, "Design of a compliant mechanism to modify an actuator characteristic to deliver a constant output force," *J. Mech. Design* **128**, 1101–1112 (2006).
[14] Y. H. Chen and C. C. Lan, "Design of a constant-force snap-fit mechanism for minimal mating uncertainty," *Mech. Mach. Theory* **55**, 34–50 (2012).
[15] C. H. Liu, M. C. Hsu, T. L. Chen and Y. Chen, "Optimal design of a compliant constant-force mechanism to deliver a nearly constant output force over a range of input displacements," *Soft Robot.* **7**(6), 758–769 (2020).
[16] J. C. Meaders and C. A. Mattson, "Optimization of near-constant force springs subject to mating uncertainty," *Struct. Multidiscipl. Optim.* **41**(1), 1–15 (2010).

[17] Y. L. Tian, C. K. Zhou, F. J. Wang, K. K. Lu, Y. J. Yuan, M. X. Yang and D. W. Zhang, "Design of a flexure-based mechanism possessing low stiffness and constant force," *Rev. Sci. Instrum.* **90**, 105005 (2019).

[18] T. T. Ye, J. Ling, X. Kang, Z. Feng and X. H. Xiao, "A novel two-stage constant force compliant microgripper," *J. Mech. Design* **143**, 053302 (2020).

[19] Y. L. Liu, Y. L. Zhang and Q. S. Xu, "Design and control of a novel compliant constant-force gripper based on buckled fixed-guided beams," *IEEE/ASME Trans. Mechatron.* **22**(1), 476–486 (2017).

[20] D. R. Nahar and T. Sugar, "Compliant Constant-Force Mechanism with A Variable Output for Micromacro Applications," **In:** *Proceedings of the 2003 IEEE International Conference on Robotics & Automation* (2003) pp. 318–323.

[21] Y. H. Chen and C. C.Lan, "An adjustable constant-force mechanism for adaptive end-effector operations," *J. Mech. Design* **134**, 031005 (2012).

[22] L. T. Danh and K. K. Ahn, "Active pneumatic vibration isolation system using negative stiffness structures for a vehicle seat," *J. Sound Vib.* **333**(5), 1245–1268 (2014).

[23] B. X. Ding, J. Y. Zhao and Y. M. Li, "Design of a spatial constant-force end-effector for polishing/deburring operations," *Int. J. Adv. Manuf. Technol.* **116**(11-12), 3507–3515 (2021).

[24] W. C. Wong, I. A. Azid and B. Y. Majlis, "Theoretical analysis of stiffness constant and effective mass for a round-folded beam in MEMS accelerometer," *Stroj. Vestn. J. Mech. E* **57**(6), 517–525 (2011).

[25] W. Z. Yan, Y. C. Yu and A. Mehta, "Analytical modeling for rapid design of bistable buckled beams," *Theor. App. Mech. Lett.* **9**(4), 264–272 (2019).

[26] J. S. Han, C. Mller, U. Wallrabe and J. G. Korvink, "Design, simulation, and fabrication of a quadstable monolithic mechanism with X- and Y-directional bistable curved beams," *ASME J. Mech. Des.* **129**(11), 1198–1203 (2007).

[27] G. M. Chen, H. Q. Wu, B. Li and M. Y. Wang, "Fully compliant bistable mechanisms with enhanced pitch stiffness," *Mech. Syst. Signal Process.* **161**, 107926 (2021).

[28] M. Derakhshani, N. Momenzadeh and T. A. Berfifield, "Analytical and experimental study of a clamped-clamped, bistable buckled beam low-frequency PVDF vibration energy harvester," *J. Sound Vib.* **497**, 115937 (2021).

[29] B. X. Ding, X. Li and Y. M. Li, "FEA-based optimization and experimental verification of a typical flexure-based constant force module," *Sens. Actuator A Phys.* **332**, 113083 (2021).

[30] C. W. Hou and C. C. Lan, "Functional joint mechanisms with constant-torque outputs," *Mech. Mach. Theory* **62**(10), 166–181 (2013).